



Earth-abundant insulator hydroxyapatite-based composite for full-spectrum photocatalytic degradation of 2, 4- dichlorophenol

Caizhi Lv ^a, Pengchong Jiao ^a, Hui Xin ^a, Lan Wu ^{a,*}, Gangfeng Ouyang ^b, Xiandeng Hou ^{a,c}

^a Analytical & Testing Center, Sichuan University, Chengdu, Sichuan 610064, China

^b School of Chemistry and Chemical Engineering, Sun Yat-Sen University, Guangzhou, Guangdong 510275, China

^c College of Chemistry, Sichuan University, Chengdu, Sichuan 610064, China



ARTICLE INFO

Keywords:

Insulator hydroxyapatite
Oxygen vacancies
Full-spectrum response
Charge separation channel
Large-scale production

ABSTRACT

Insulator hydroxyapatite (HAp) was chosen as a candidate to construct full-spectrum photocatalyst. Glucose as a functional precursor was incorporated into HAp by coprecipitated method, and the glucose-modified HAp was then calcined under nitrogen atmosphere. With the loss of OH⁻ group in HAp and the decomposition of glucose during the calcination, oxygen vacancies (OVs) for regulating the band gap, graphitic carbon (GC) as a good electron acceptor, and a channel for rapid carrier separation via the C-O-Ca forming between OV-HAp and GC can be simultaneously achieved. The as-prepared OV-HAp/GC displayed full-spectrum response and rapid separation of carriers. Moreover, it showed high degradation performance for 2, 4-dichlorophenol (2, 4-DCP), phenol, and tetracycline under visible, NIR, and full-spectrum. This strategy is not only facile, but also exhibits a certain universality. This work opens a new window for full-spectrum photocatalysts construction based on insulators, and large-scale production for practical use can be expected.

1. Introduction

In recent years, the design of full-spectrum photocatalyst has attracted widespread attention because of their ability to harvest the entire solar spectrum. To date, taking use of their inherently narrow band gap, semiconductor materials have been utilized to construct the photocatalysts with full-spectrum response for the degradation of organic contaminants [1–6]. However, semiconductor materials are relatively rare, expensive and the preparation process of the semiconductor-based photocatalysts were also tedious, which are not conducive to large-scale production and limit their practical application [7]. By contrast, the earth-abundant insulator materials exhibit various merits of economic advantage, robust chemical stability and easy availability [8]. Moreover, some studies revealed that the insulator materials could be endowed with photocatalytic activities through regulating their compositions and structure for decreasing their band gap [9–13]. Therefore, it is potential to use insulators as the original materials to develop full-spectrum photocatalysts. Besides, through simplifying the construction process, the preparation of low-cost and large-scale photocatalysts based on insulators can be expected.

Among the insulators, hydroxyapatite (HAp), a significant inorganic functional material widely available in nature, has advantages of good

thermal stability, low price, and environmental friendliness [14,15], thus receiving increased attention in the photocatalysis domain in the past few decades. In order to narrow down its wide band gap (6.0 eV) [15], researchers modified HAp by ion doping, making it show good UV or visible photocatalytic performance [10,16,17]. In our previous work [18,19], we constructed oxygen vacancies (OVs) in HAp by simply calcining it under air atmosphere. This introduced new defect energy levels into HAp, decreasing its band gap and broadening the light absorption range to the visible region. These studies suggested that HAp can be used as a good candidate for development of the insulator-based photocatalysts. Further, the single-phase HAp was composited with another material to fabricate biphasic heterojunction, thereby facilitating the separation of photo-generated charges, such as g-C₃N₄/HAp, Ag₃PO₄/HAp and HARCP/HAp [20–23]. Nevertheless, the light response of the reported HAp-based photocatalysts were hard to response in the near-infrared (NIR) region and the preparation still need several steps. These hindered its application for construction of full-spectrum photocatalyst. To address these issues, we suppose that if the generation of OVs with high concentration, introduction of electron acceptor, and construction of the channel for photo-generated charges separation can be simultaneously achieved based on calcination of HAp, the large-scale production of HAp-based full-spectrum photocatalysts

* Corresponding author.

E-mail address: wulan@scu.edu.cn (L. Wu).

for practical use can be anticipated in the future.

Previous reports indicated that the glucose as a cheap organic material widely distributed in nature, showing a role in regulation of OV generation on the semiconductors and preparation of the graphitic carbon (GC) [24,25]. Zhou et al. introduced glucose into $\text{Bi}/\text{Bi}_2\text{O}_{2-x}\text{CO}_3$ via the simple hydrothermal method. They found that the generated intermediates ($\text{C}_{60}\text{H}_{102}\text{O}_{51}$) from the hydrothermal reaction of glucose reduced the Bi^{3+} into Bi^0 , introducing OV on $\text{Bi}_2\text{O}_{2-x}\text{CO}_3$ and thereby narrowing its band gap [26]. Similarly, Zhu's team prepared the biphasic TiO_2 /graphite-like carbon layer composite by using glucose as carbon resource via hydrothermal method. They proposed that the formation of graphite-like carbon layer, a good electron acceptor, effectively promoted the carrier separation [27]. Inspired by these work, it was possible to achieve the goal for construction of the efficient HAp-based full-spectrum photocatalyst through incorporation of glucose as a functional precursor into HAp.

Herein, we introduced glucose into HAp by coprecipitated method, making the glucose-modified HAp complex. This complex was calcined under nitrogen (N_2) atmosphere, obtaining the OV-HAp/GC composite photocatalyst, simultaneously showing full-spectrum response and rapid separation of carriers. Specifically, glucose-modified HAp was calcined under N_2 atmosphere to obtain OV-HAp material with abundant OVs. The formed OVs introduced new defect energy levels into OV-HAp, making it show NIR light response. Simultaneously, the GC was generated from decomposition of glucose during the calcination, accompanying with formation of a channel for rapid carrier separation through the C-O-Ca covalent bond in the interface between OV-HAp and GC. The as-prepared OV-HAp/GC catalyst displayed high photocatalytic degradation for 2, 4-dichlorophenol (2, 4-DCP), phenol, and tetracycline under visible, NIR, and full-spectrum. Among them, the degradation rates for 2, 4-DCP were 1.8×10^{-3} , 9.8×10^{-4} and 0.15 min^{-1} , respectively. Therefore, the OV-HAp/GC photocatalyst displayed huge promising for future practical application.

2. Experimental sections

2.1. Materials

2, 2, 6, 6-Tetramethylpiperidine (TEMP), 2, 4-dichlorophenol (2, 4-DCP) and phenol were purchased from Aladdin Reagent Co. (Shanghai, China). Tetracycline (TC), calcium chloride anhydrous (CaCl_2), diammonium hydrogen phosphate ($(\text{NH}_4)_2\text{HPO}_4$), sodium hydroxide (NaOH), glucose anhydrous ($\text{C}_6\text{H}_{12}\text{O}_6$), sodium sulfate anhydrous (NaSO_4), ethylenediaminetetraacetic acid disodium salt dihydrate (EDTA), Tryptophan (Trp), isopropyl alcohol (IPA), and benzoquinone (BQ) were purchased from Kolon Reagent Factory (Chengdu, China). 5, 5-Dimethyl-1-pyrroline N-oxide (DMPQ) was purchased from Dojindo Co. (Shanghai, China). All reagents were analytical grade and used without further purification.

2.2. Preparation of the glucose-modified hydroxyapatite

Glucose-modified hydroxyapatite was prepared according to the reported "molecular cage" method [28]. Generally, 1109.8 mg anhydrous CaCl_2 (10 mmol) and 792.4 mg $(\text{NH}_4)_2\text{HPO}_4$ (6 mmol) were dissolved into 100 mL deionized water and sonicated for 10 min, respectively. The $(\text{NH}_4)_2\text{HPO}_4$ solution was dropwise added into the CaCl_2 solution with magnetic stirring, then obtaining a milky white suspension. The pH value of the mixed solution was adjusted to 3.5 with 1.0 mol/L HCl solution and donated as A solution. 15.0 g glucose and 1.5 g NaOH were dissolved into 50 mL deionized water, accordingly. The two solutions were mixed and sonicated for 10 min, labeled as solution B. Solution A was dropwise added into solution B with magnetic stirring. The mixture was aged for 8 h making the white precipitate completely sink. The obtained precipitate was washed with deionized water and anhydrous ethanol, which was then separated by centrifugation. Finally, the

glucose-modified hydroxyapatite was obtained after drying at 100 °C, which was donated as 15GHAp. The amount of anhydrous glucose was adjusted ($m = 5, 10, 20$ and 25 g) to obtain 5GHAp, 10GHAp, 20GHAp and 25GHAp according to the above steps. The CaSiO_3 insulator material modified by glucose were prepared via the similar process to that of 15GHAp, and obtained 15GCaSiO₃, seen in SI 1.1.

2.3. Preparation of OV-HAp/GC, OV-HAp and GC

15GHAp was placed in the tube furnace and purged with N_2 for 20 min, ensuring that the air in the quartz tube was completely removed. Then, the temperature of the tube furnace was increased from room temperature to 500 °C at a rate of 4 °C/min and maintained at 500 °C for 1 h. After the calcination process, the tube furnace was cooled to room temperature. The obtained black product was donated as OV-HAp/GC. As comparison, anhydrous glucose was calcined under the identical condition to OV-HAp/GC to get pure GC. Besides, the 15GHAp was calcined under air atmosphere to obtain OV-HAp. The specific preparation procedure was described in Fig. S1. For the 15GCaSiO₃, the calcination process was shown in SI 1.2.

2.4. Catalyst characterization

The phase and crystallinity of samples were determined by an EMPYREAN (Panalytical, Netherlands) powder X-ray diffraction (PXRD) using $\text{Cu K}\alpha$ radiation with the scanned range from 10° to 80°. The morphologies and microstructures of the samples were investigated by transmission electron microscope (TEM, Tecnai G2 F20, FEI, USA), and the average particle size of the samples was obtained by counting the size distribution of 100 nanoparticles in the TEM images of OV-HAp and OV-HAp/GC using nano measurer version 1.2 software. The elemental distribution of samples was obtained by the scanning electron microscopy (SEM, JEOL, Japan) on a JSM-7500 F apparatus equipped with an energy dispersive spectroscopy (EDS). Brunauer-Emmett-Teller (BET) specific surface area and pore size of samples were measured by N_2 physical adsorption at -196 °C on the ASAP 2020 instrument (Micromeritics, USA). The infrared spectra of the samples were recorded using a Nicolet 6700 Fourier transform infrared spectrometer (FT-IR, Thermoelectronics, USA) with scanned range from 4000 to 400 cm^{-1} . Raman spectra were obtained on a LabRAM HR Raman spectrometer (HORIBA, France). The applied wavelength of laser light was 532 nm with the collected range from 4000 to 150 cm^{-1} . The thermal stability of the 15GHAp was analyzed by the DSC2 thermogravimetric analyzer (TGA, Mettler Toledo, Netherlands). The sweeping temperature range was 32–620 °C, temperature accuracy was ± 0.1 °C, thermal accuracy was $\pm 0.05\%$, thermal sensitivity was 0.04 μW , and heating rate was 0.3 °C/min. The oxygen vacancies of samples were carried out by the EMXplus X-band electron paramagnetic resonance (EPR) spectrometer (Bruker, Germany) at room temperature. The surface chemical state of samples was analyzed using AXIS Ultra DLD clutches X-ray photoelectron spectroscopy (XPS, Kratos, UK). The UV-vis diffuse reflectance spectra (UV-vis DRS) of the samples were measured using the UV 3600 spectrophotometer (Shimadzu, Japan). The scanned range was from 200 to 1500 nm and BaSO_4 was used as the reference for baseline correction. The band gap (E_g) of photocatalysts was calculated according to the formula $E_g = 1240/\lambda$, in which λ was the maximum light absorption edge of the photocatalysts [29]. Photoluminescence (PL) spectra were acquired at room temperature by F-7000 (Hitachi, Japan) with an excitation wavelength of 405 nm [30]. Both incident and emission slits were 5.0 nm, the photomultiplier voltage was 700 V, and the scanning wavelength was from 420 to 600 nm.

2.5. Electrochemical testing

Electrochemical impedance spectroscopy (EIS), photocurrent density, and Mott-Schottky (M-S) curves of the samples were acquired in the

electrochemical workstation equipped with three electrodes (AUTO LAB PGSTAT302N, Netherlands). Generally, 1 mg sample was dispersed into a mixed solvent with 373 μ L deionized water and 125 μ L isopropanol. Then, 10 μ L nafion solution was added into the above solution and sonicated uniformly. 50 μ L sample suspension was taken out and coated on the indium tin oxide (ITO) electrode, which was then dried and used as the working electrode. The Pt was used as the counter electrode and Ag/AgCl was the reference electrode. The M-S curves of the samples were tested in 0.2 mol/L Na₂SO₄ solution to obtain the flat-band potential. A xenon lamp with different wavelength filters was used as the light source to collect the EIS spectra of the samples in the visible, NIR, and full-spectrum light in the range of 0.1–10⁵ Hz. In addition, the photocurrent signals of the above photocatalysts under the visible, NIR, and full-spectrum light were recorded at an external voltage of 0.3 V with the light source turned on/off at 20 s intervals.

2.6. Theoretical calculations

The density functional theory (DFT) calculation was performed by Vienna Ab initio Simulation Package (VASP) [31] with the projector augmented wave (PAW) method [32]. The exchange function was treated using the generalized gradient approximation (GGA) of the Perdew-Burke-Ernzerhof (PBE) formulation [33]. The energy cutoff for the plane wave basis expansion was set to 450 eV and the force on each atom less than 0.05 eV/Å was set for the convergence criterion of geometry relaxation. Grimme's DFT-D3 methodology [34] was used to describe the dispersion interactions. Partial occupancies of the Kohn-Sham orbitals were allowed using the Gaussian smearing method with a width of 0.05 eV. The Brillouin zone was sampled with Monkhorst mesh $3 \times 3 \times 1$ through the computational process. The self-consistent calculations were applied a convergence energy threshold of 10⁻⁵ eV. The 15 Å vacuum space along the z direction was added to avoid the interaction between the two neighboring images.

2.7. Photocatalytic activity evaluation

2.7.1. Photocatalytic degradation of pollutants

The photocatalytic activity of the prepared photocatalysts were investigated by degradation of 2, 4-DCP under visible (400–800 nm), NIR (> 800 nm) and full-spectrum light irradiation. A xenon lamp (PLS-SXE 300, Beijing Perfectlight Technology Co., Ltd.) with a light intensity of about 260 mW/cm² was placed 10 cm above the photocatalysts as the incident light source for photocatalytic degradation. Generally, 25 mg OV-HAp/GC was added into 50 mL, 5 mg/L 2, 4-DCP aqueous solution. Then, the mixed system kept stirring in the dark for 30 min to achieve the adsorption equilibrium. During the illumination process, 2 mL solution was collected at a certain time for analysis. The photocatalytic degradation efficiency was measured by using the UH 5300 UV-vis spectrophotometer (Hitachi, Japan) with the characteristic absorption peak of 286 nm [35]. In addition, the photocatalytic degradation of phenol (5 mg/L) and TC (20 mg/L) by OV-HAp/GC was also investigated under the identical conditions to that of OV-HAp/GC. Moreover, the degradation performance of OV-HAp/GC for TC was studied under natural sunlight irradiation. The photocatalytic degradation efficiency (D%) of above contaminants (2, 4-DCP, phenol and TC) were calculated as follows:

$$D(\%) = \frac{C_0 - C_t}{C_0} \times 100\%$$

where C₀ and C_t represented the initial concentration of the contaminant and the concentration of the contaminant after being irradiated for a certain period of time (t), respectively.

2.7.2. Detection of photocatalytic degradation of 2, 4-DCP intermediates

The intermediates detection in the 2, 4-DCP degradation process was

performed on the liquid chromatograph-mass spectrometer (LC-MS, Thermo Fisher Scientific, San Jose, CA) equipped with a heated electrospray ionization source. The mobile phase was the mixed solution containing methanol and water with a volume ratio of 70/30, the injection flow rate was 1 mL/min, and the detector wavelength was 286 nm.

3. Results and discussion

3.1. Chemical composition and microstructure

In Fig. 1A, the PXRD pattern of GC showed two diffraction peaks at 22.9° and 44.5°, corresponding to the (002) and (101) crystal planes of the graphitized carbon layers [36]. For 15GHAp, OV-HAp and OV-HAp/GC, they presented the identical characteristic diffraction peaks to the standard HAp (no. 09-0432). The corresponded crystal planes were (002), (211), (112), (300), (202), (310), (222), (213) and (004) (Fig. 1A and Fig. S2), respectively, suggesting that both the introduction of glucose and calcination hardly changed the phase composition of HAp. Notably, the diffraction peak at 22.9° for the GC (002) crystal plane was also observed on OV-HAp/GC sample, demonstrating the synthesis of composite photocatalytic materials. However, the crystallinity of OV-HAp/GC was decreased compared with that of OV-HAp due to its full-width at half-maximum (FWHM) was wider than that OV-HAp (Table S1), manifesting that the introduction of GC led to a more disordered OV-HAp lattice with more defects [37]. In order to obtain the weight ratios of OV-HAp and GC in OV-HAp/GC, the C element weight percentage of OV-HAp/GC, as well as the weight ratio of P element were firstly tested by EDS and titration analysis method. Then, the weight ratios of OV-HAp and GC were estimated according to the above results shown in Table S2. Apparently, the results from both the EDS and titration analysis were consistent. Namely, the weight ratio of GC in the OV-HAp/GC composites increased with the amount of the introduced glucose increasing from 5 g to 15 g, and reached the maximum (GC: ~10%, OV-HAp: ~90%) when the glucose dosage was 15 g. However, with the amount of the glucose further increasing, the content of GC decreased. These results indicated that the contents of OV-HAp and GC in the composites were affected by the introducing of glucose, and the weight ratios of these two phases could be regulated through adjusting the glucose dosage.

The specific surface area of OV-HAp and OV-HAp/GC were 41.3 and 55.7 m²/g, accordingly (Table S3). The slightly larger surface area of OV-HAp/GC than that of OV-HAp may show the advantage for contaminant adsorption. The N₂ adsorption-desorption isotherms of OV-HAp and OV-HAp/GC samples all presented type IV curves [38], and the corresponded pore sizes were 27.9, and 28.7 nm, respectively, indicating that they are mesoporous. Moreover, the morphology and microstructure of the samples were characterized by TEM and HRTEM. For GC, its morphology was an irregular block structure with a mean interlayer distance of 0.35 nm (Fig. S3). TEM images of OV-HAp and OV-HAp/GC showed that they had similar nanorod structures (Fig. 1B–C), whereas the particle size of HAp in OV-HAp/GC was smaller (13.8 nm) than that in OV-HAp (23.9 nm) (Fig. S4). This decreased particle size of HAp was possibly caused by its decreased crystallinity according to the PXRD results. The HRTEM images of OV-HAp and OV-HAp/GC were given in Fig. 1D–G. The lattice fringe of 2.78 Å was observed on the two samples, which corresponded to the (112) crystal plane of OV-HAp. This confirmed the successful preparation of HAp, being consistent with the PXRD results. Interestingly, an interface between the OV-HAp (112) crystal plane and GC was observed on the OV-HAp/GC sample (Fig. 1F). Meanwhile, GC, as an electron receptor, which was beneficial to the transfer of photoelectrons [27,39]. Thus, we speculated that there might be an interfacial interaction between the two phases [40].

The FT-IR results of GC, OV-HAp and OV-HAp/GC were presented in Fig. 2A–B. For GC, the bands at 3423, 1731, 1621, 1378 and 1050 cm⁻¹

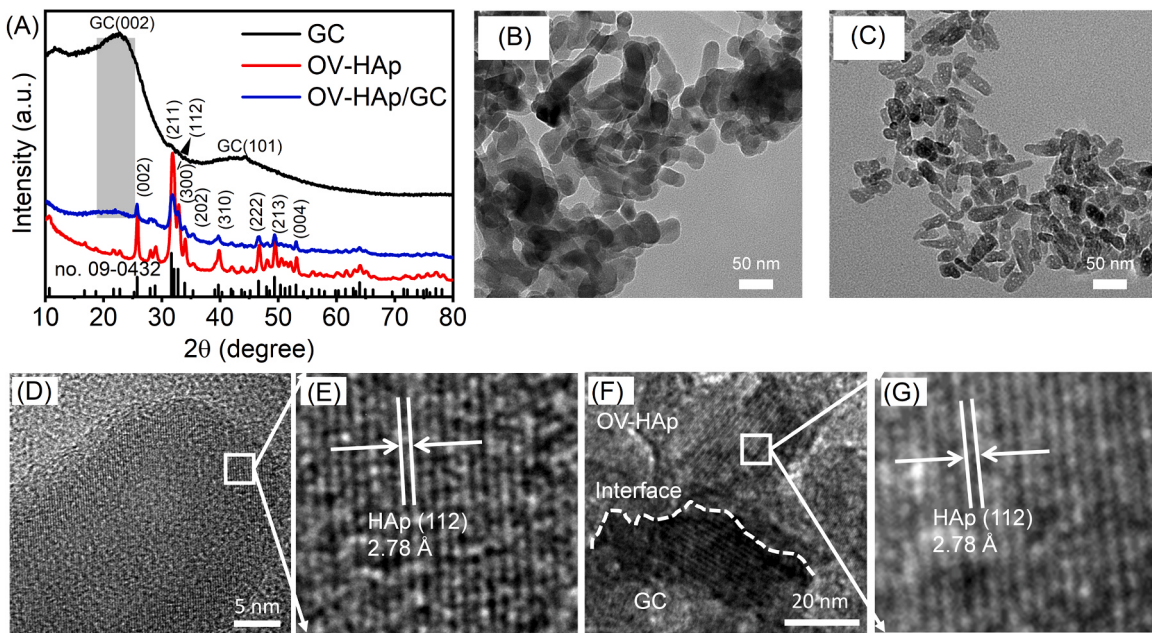


Fig. 1. Crystal structure and morphology characterization of the as-prepared photocatalysts. PXRD patterns of GC, OV-HAp, and OV-HAp/GC samples (A). TEM images of OV-HAp (B) and OV-HAp/GC (C). HRTEM images of OV-HAp (D, E) and OV-HAp/GC (F, G).

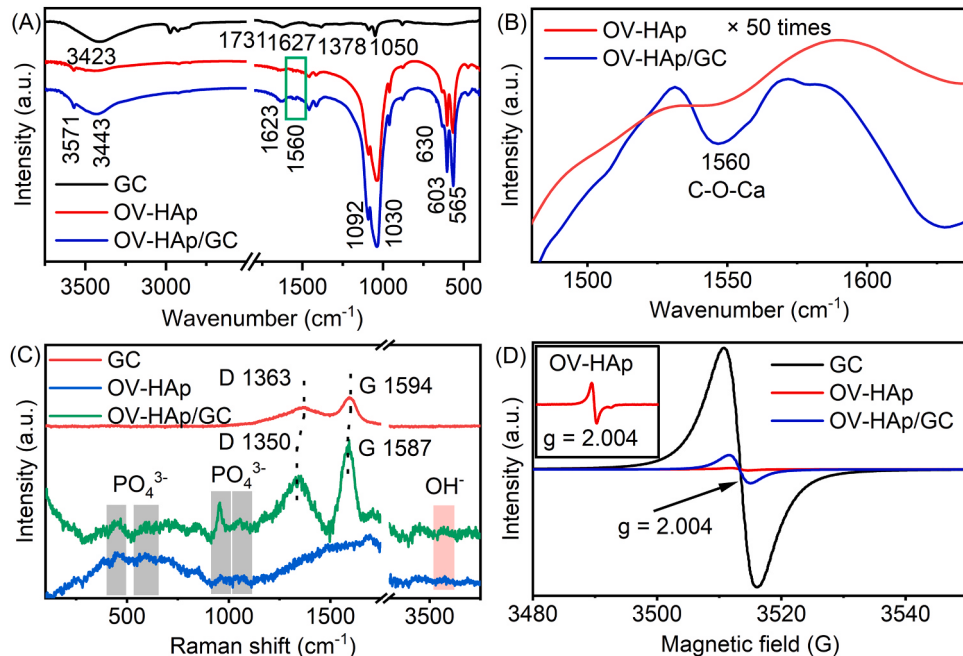


Fig. 2. Identification of the functional groups and oxygen vacancies on the photocatalysts. FT-IR spectra of GC, OV-HAp, and OV-HAp/GC (A). (B) was the enlarged 50 times of both OV-HAp and OV-HAp/GC in figure (A). Raman spectra (C), and EPR spectra (D) of GC, OV-HAp and OV-HAp/GC.

were associated to the O-H, C=O, C=C, C-OH and C-O vibration, accordingly [41] (Fig. 2A). In the case of OV-HAp, the bands at 3571 and 630 cm^{-1} [42,43] were the vibration of OH^- groups in HAp, 1092, 1030, 603, and 565 cm^{-1} were the characteristic peaks of PO_4^{3-} . For OV-HAp/GC, the characteristic peaks of PO_4^{3-} and OH^- attributed to OV-HAp also appeared. Besides, the vibrational peaks of O-H (3443 cm^{-1}) and C=C (1623 cm^{-1}) in GC were found on OV-HAp/GC sample, further demonstrating the successful preparation of OV-HAp/GC. Notably, a new peak with weak intensity at 1560 cm^{-1} was observed on OV-HAp/GC (Fig. 2B). According to the reported work, we assigned this peak to the C-O-Ca covalent bond, which might be

generated from the interfacial reaction between the oxygen-containing group of GC and the Ca atom of OV-HAp [44].

Raman spectroscopy analysis was performed to investigate the functional groups of the samples and validated the interfacial interaction in OV-HAp/GC. As shown in Fig. 2C, four characteristic peaks of PO_4^{3-} appeared at 430, 590, 960, and 1047 cm^{-1} on OV-HAp and OV-HAp/GC [45]. However, the OH^- characteristic peak belonged to HAp at 3570 cm^{-1} on OV-HAp/GC and OV-HAp almost disappeared compared with that on 15GHAp (Fig. S5), indicating that some OH^- groups escaped from the lattice of HAp during the calcination process. Besides, the TGA results also confirmed this phenomenon, which

showed that 15GHAp had three stages of weight loss. The physisorbed and chemisorbed water on HAp were lost in stages I (40–130 °C) and II (130–250 °C), respectively. The weight loss in stage III (250–500 °C) was attributed to the decomposition of glucose on HAp and the loss of OH[−] groups from the HAp lattice (Fig. S6) [46]. Moreover, the bands at 1363 and 1594 cm^{−1} for GC (Fig. 2C) were ascribed to the D-band disordered carbon (sp³) and G-band graphitic carbon (sp²), respectively [47]. For OV-HAp/GC, the D-band and G-band characteristic peaks of GC shifted to the lower wavenumber (1350 and 1587 cm^{−1}). It manifested that there was an intensive interaction between GC and OV-HAp [48], being in agreement with the HRTEM and FT-IR results. The intensity ratio of D-band and G-band (I_D/I_G) on OV-HAp/GC was 0.6, suggesting that it had a good graphitization and thus could display fast transfer ability for the photogenerated electrons [49].

EPR measurement was employed to characterize the generation of oxygen vacancies, as shown in Fig. 2D. The oxygen vacancy signal was observed at $g = 2.004$ on GC, OV-HAp and OV-HAp/GC [37,50,51], and the corresponded signal intensity decreased in the order of GC > OV-HAp/GC > OV-HAp. The strongest oxygen vacancy signal for GC was due to the abundant hydroxyl functional groups on the glucose surface, which underwent dehydration polymerization reactions during calcination and thus generated a large number of defects [52,53]. For OV-HAp/GC, the escaped OH[−] groups from the HAp lattice shown in Raman results introduced the oxygen vacancies [46,54]. Its weak OV intensity might be due to the lower content of OH[−] groups on 15GHAp than that on glucose. For OV-HAp, the weaker OV signal of OV-HAp than that of OV-HAp/GC was due to that the generated oxygen vacancies was easier to be filled by oxygen molecules in air than that in N₂ (Fig. 2D inset) [55].

The XPS survey spectra and the corresponding high-resolution (HR) XPS spectra of the samples were collected shown in Fig. 3 and Fig. S7. The fitted peaks of O 1s spectra at 531.2, 531.9 and 532.2 eV were attributed to lattice oxygen, oxygen species adsorbed in oxygen vacancies, and adsorbed water, accordingly [56–58]. These further confirmed the presence of oxygen vacancies in both OV-HAp and OV-HAp/GC samples [59] (Fig. 3A). Based on the O 1s HRXPS results, we calculated the surface content of oxygen vacancies [58,60]. The surface oxygen vacancies content in the OV-HAp/GC (28.7%) was higher than that of OV-HAp (14.0%), indicating that OV-HAp/GC contained abundant oxygen vacancies and thus can introduce more defect levels. Interestingly, the fitted peaks of O 1s, Ca 2p, and P 2p of OV-HAp/GC all shifted toward higher binding energy compared to those of OV-HAp (Fig. 3A–C), while the O 1s spectra shifted toward lower

binding energy compared to that of GC (Fig. S7 B). These results implied that the photoelectrons of OV-HAp transferred to GC through the C-O-Ca bond [61], which further validated the interfacial interaction between OV-HAp and GC.

3.2. Photoelectrochemical properties

The UV-vis DRS spectra of the OV-HAp and OV-HAp/GC were depicted in Fig. 4A–B. The absorption edge of OV-HAp was approximately at 1000 nm (Fig. 4A), corresponding to the band gap (E_g) of 1.24 eV based on the Tauc plots (inset of Fig. 4A) calculated via the Kubelka-Munk method [62]. The band gap of OV-HAp was smaller than that of pure HAp (6.0 eV) [15], which was due to the defect energy levels introduced after oxygen vacancies generation. The optical absorption range of OV-HAp/GC increased to 1200 nm compared to that of OV-HAp, corresponding to a band gap of 1.03 eV (Fig. 4B and inset). The enlarged absorption range for OV-HAp/GC was probably ascribed to the higher content of oxygen vacancies compared with that of OV-HAp, which enhanced its NIR responsive ability [63,64]. The Mott Schottky curves (M-S) of OV-HAp (Fig. 4C) and OV-HAp/GC (Fig. 4D) displayed that all the linear plots possessed positive slopes, demonstrating that both of them were the n-type semiconductors [62]. Based on the M-S curves and the intercept of the x-axis, the flat band potential (E_{fb}) of both OV-HAp and OV-HAp/GC were −0.60 V (vs Ag/AgCl), and they were equivalent to −0.36 V versus the normal hydrogen electrode (NHE). The conduction band (CB) minimum potential (E_{CB}) of n-type semiconductors was usually more negative by about 0.1 V than the E_{fb} [65]. Thus, the E_{CB} potentials of OV-HAp and OV-HAp/GC were −0.46 V. According to E_g = E_{VB} − E_{CB}, the E_{VB} of OV-HAp was obtained as 0.78 V. Since the redox potential of E_{CB} was more negative than that of E (O₂/•O₂) = −0.33 V, it indicated that the electrons located on CB could react with O₂ to form •O₂ radicals [66], thus facilitating the photocatalytic reaction.

The separation and transfer efficiency of photogenerated charges were crucial factors for evaluating photocatalytic performance [67]. As shown in Fig. 5A, the PL emission spectrum of OV-HAp/GC showed the weakest intensity compared to those of GC and OV-HAp, indicating that OV-HAp/GC had the strongest ability to inhibit the electron-hole pair recombination. Moreover, electrochemical impedance spectroscopy (EIS) and transient photocurrent measurements were also conducted for the comprehensive study of the photo-response ability and photogenerated charges recombination efficiency of the photocatalyst [68]. As shown in Fig. 5B, the EIS results showed that the arc radius of

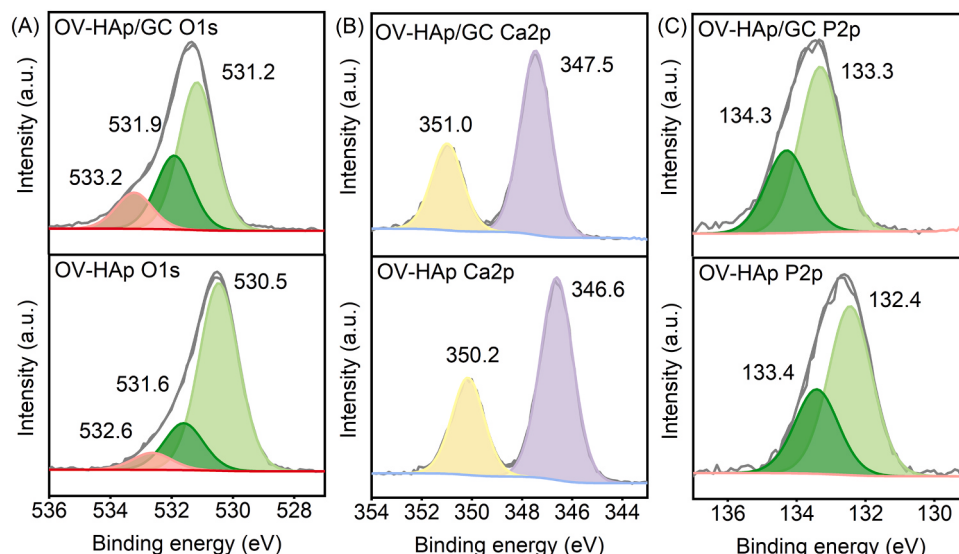


Fig. 3. High-resolution XPS spectra of OV-HAp and OV-HAp/GC samples. O 1s (A), Ca 2p (B), P 2p (C) spectra.

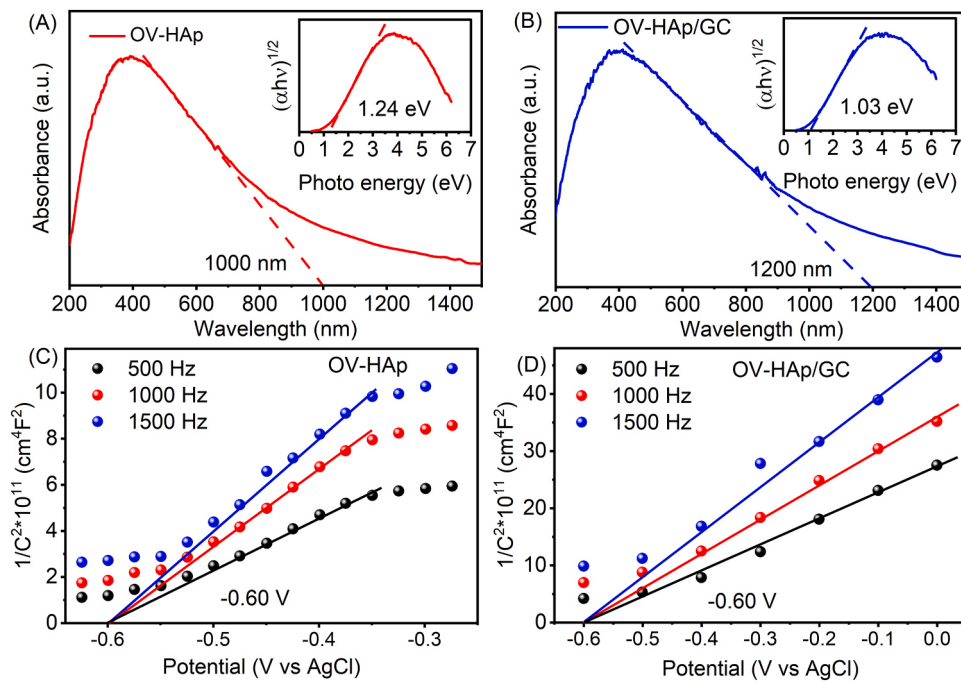


Fig. 4. UV-vis DRS spectra of different photocatalysts and the corresponded Tauc curves. OV-HAp (A, inset) and OV-HAp/GC (B, inset), as well as the M-S curves of OV-HAp (C) and OV-HAp/GC (D).

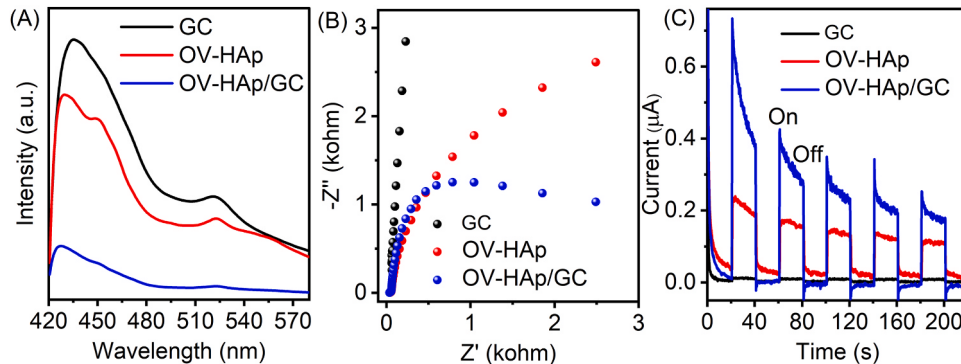


Fig. 5. Photogenerated carrier separation characterization of the photocatalysts. PL spectrum (A), EIS (B), transient photocurrent response (C).

OV-HAp/GC was the smallest, which possessed the highest interface charge separation and transfer efficiency. Besides, OV-HAp/GC exhibited the highest current density among all samples (Fig. 5C), manifesting that it had the lowest photogenerated charges recombination efficiency. The smallest arc radius (Fig. S8A and Fig. S8C) and the strongest photocurrent (Fig. S8B and S8D) were also observed on OV-HAp/GC under visible and NIR light irradiation. These results indicated that the incorporation with GC helped to separate the electron-hole pairs generated on OV-HAp.

3.3. Evaluation of the photocatalyst performance

The relevant parameters of the degradation experiment on OV-HAp/GC were optimized before evaluating the photocatalytic performance of the samples (Fig. S9–S12). Under optimal conditions, the photocatalytic activities of GC, OV-HAp and OV-HAp/GC were evaluated by degrading 2, 4-DCP aqueous solution under visible, NIR, and full-spectrum light irradiation, accordingly, as presented in Fig. 6A–C. The self-degradation of 2, 4-DCP was almost negligible under the above three light irradiation. Under visible light, the degradation efficiency of 2, 4-DCP on OV-HAp/GC was 49%, whereas those for GC and OV-HAp was 13% and

23%, respectively (Fig. 6A). This was ascribed to the stronger photogenerated electron-hole pair separation ability of OV-HAp/GC than those of GC and OV-HAp. The similar phenomenon was observed under NIR light. The degradation efficiency of 2, 4-DCP on OV-HAp/GC was the highest (44%), which was 6.3 and 2.9 times higher than those on GC (7%) and OV-HAp (15%), respectively (Fig. 6B). Moreover, the degradation efficiency of 2, 4-DCP on OV-HAp/GC reached 99% under the full-spectrum light irradiation for 40 min, which was 6.6 and 3.2 times higher than those on GC (15%) and OV-HAp (31%), respectively (Fig. 6C). In addition, we compared the degradation efficiency of the OV-HAp/GC composite and the mechanically mixed sample of OV-HAp and GC (denoted as OV-HAp/GC-MM). The degradation efficiency of OV-HAp/GC for 2, 4-DCP was higher than that of OV-HAp/GC-MM under the identical measurement conditions (Fig. S13). This confirmed that the interfacial interaction between OV-HAp and GC played a predominant role in the photocatalytic activity enhancement.

The OV-HAp and OV-HAp/GC samples were also used in the cycled experiments to evaluate their photocatalytic stability. As shown in Fig. S14A, the photocatalytic activity OV-HAp/GC remained above 95% (Fig. S14A, red line) after five cycles, while that of OV-HAp significantly declined from 32% to 21% (Fig. S14A, black line). Moreover, the XRD

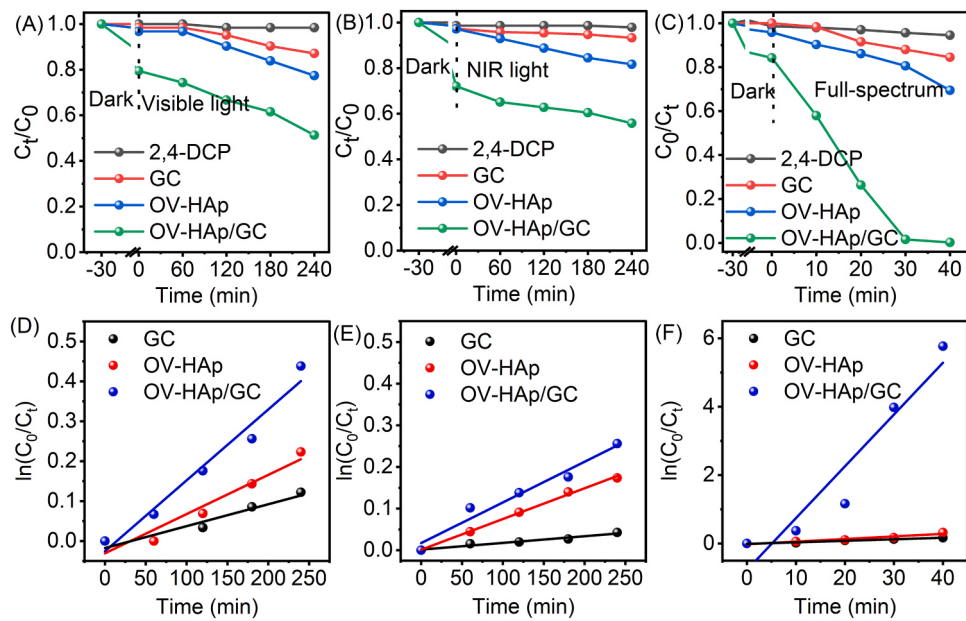


Fig. 6. Photocatalytic performance of different photocatalysts for degradation of 2, 4-DCP under different lights irradiation. Visible light (A), NIR light (B) and full-spectrum (C). The reaction rate of 2, 4-DCP on different photocatalysts under visible light (D), NIR light (E) and full-spectrum (F).

and FT-IR results showed that the structure of OV-HAp/GC samples after 5 cycles experiments hardly changed compared with the fresh one (Fig. S14B and Fig. S14C). The above results implied that the OV-HAp/GC was a good and stable photocatalyst for degradation of 2, 4-DCP.

Furthermore, the photocatalytic degradation kinetics of 2, 4-DCP on different photocatalysts under visible, NIR, and full-spectrum light were investigated (Fig. 6D-F). The results showed that the changes in 2, 4-DCP concentration versus the reaction time on different photocatalysts followed a pseudo-first-order kinetics equation [69]:

$$\ln(C_0/C_t) = k_{app} \cdot t$$

where t was the irradiation time, C_0 and C_t were the initial concentration of 2, 4-DCP and the concentration at t min of light exposure, respectively. The k_{app} was the apparent rate constant of the pseudo-first-order equation. Fig. 6D-F displayed that OV-HAp/GC had the maximum rate constant of $1.8 \times 10^{-3} \text{ min}^{-1}$, $9.8 \times 10^{-4} \text{ min}^{-1}$ and 0.15 min^{-1} in the visible, NIR and full-spectrum light, which was 1.8, 1.3 and 20 times higher than those on OV-HAp, accordingly. In addition, the photocatalytic degradation of both phenol and tetracycline (TC) by OV-HAp/GC were also investigated (Fig. S15-S17). The results showed that OV-HAp/GC could not only efficiently degrade phenol (Fig. S15), but also rapidly degraded TC under visible, NIR, full-spectrum light and natural sunlight (Fig. S16 and Fig. S17). We further compared the photocatalytic performance of OV-HAp/GC with the reported full-spectrum photocatalysts. The OV-HAp/GC showed a full-spectrum photocatalytic performance superior to most of the previously reported work (Table S4-S6), indicating a promising application of OV-HAp/GC for photocatalytic degradation of organic contaminants.

3.4. Theoretical calculations

3.4.1. Band gap calculation for OV-HAp

According to the experimental results, the structure models for calculation of oxygen vacancies generated energy level were constructed by removal of an oxygen atom in the PO_4^{3-} and OH^- groups, as well as removal of the entire OH^- group in the crystalline plane of OV-HAp (112) (denoted as OV-HAp-1, OV-HAp-2, OV-HAp-3, accordingly, as shown in Fig. S18). The band gaps of the three models were subsequently calculated by DFT simulation, which was decreased to 3.39 eV, 3.44 eV and

0.25 eV compared with HAp (6.0 eV), accordingly (Fig. 7A), and the corresponded optical absorption wavelengths were 366, 344 and 4960 nm. Among them, the optical absorption range of OV-HAp-3 covered the entire solar spectrum [11].

3.4.2. Calculation of the TDOS and PDOS of OV-HAp

The total density of states (TDOS) and partial density of states (PDOS) of them were calculated by DFT to explain the decreased band gap of three OV-HAp models, (Fig. 8, Fig. S19 and Fig. S20). In Fig. 8A, the electronic structures of the three OV-HAp models showed that new defect energy levels appeared compared with HAp (Fig. 8A black line). In particular, the OV-HAp-3 model generated the most defect energy levels among all models. This resulted in the lowest band gap after the loss of OH^- group in OV-HAp (112) plane, which was consistent with the previous reports [11]. Specifically, the generated defect energy levels were not only formed in the p orbitals of O atoms (Fig. 8B), but also in the d orbitals of Ca atoms (Fig. 8C). Besides, the energy bands of the P and H atoms in OV-HAp-3 all shifted to the lower energy region compared to HAp (Fig. 8D-E) [9], manifesting the formation of new defect energy level. Unlike OV-HAp-3, the defect energy levels of OV-HAp-1 mainly appeared in the p orbitals of both O and P atoms (Fig. S19), while those for OV-HAp-2 mainly appeared in the d orbitals of Ca atoms and the s orbitals of H atoms (Fig. S20).

3.4.3. Interfacial charge transfer

To validate the interfacial charge transfer between OV-HAp and GC, the interfacial structure model was constructed. It mainly consisted of Ca atoms in OV-HAp and O atoms in GC, forming a Ca-O bond with a bond length of 2.57 Å in the interface section according to the HRTEM and FT-IR results [70], as shown in Fig. 9A. The electron localization function results showed that there was a covalent interaction between the Ca atoms in OV-HAp and the O atoms in GC (Fig. 9B). This corroborated the formation of a covalent bond between the OV-HAp and GC [71], which was in agreement with the FT-IR results. Besides, the differential charge density of OV-HAp/GC showed the charge depletion of Ca atoms in OV-HAp (blue) and the charge accumulation of O atoms in GC (yellow) (Fig. 9C), which strongly confirmed that the electrons generated by photoexcitation were transferred from OV-HAp to GC, being consistent with the XPS results (Fig. 3).

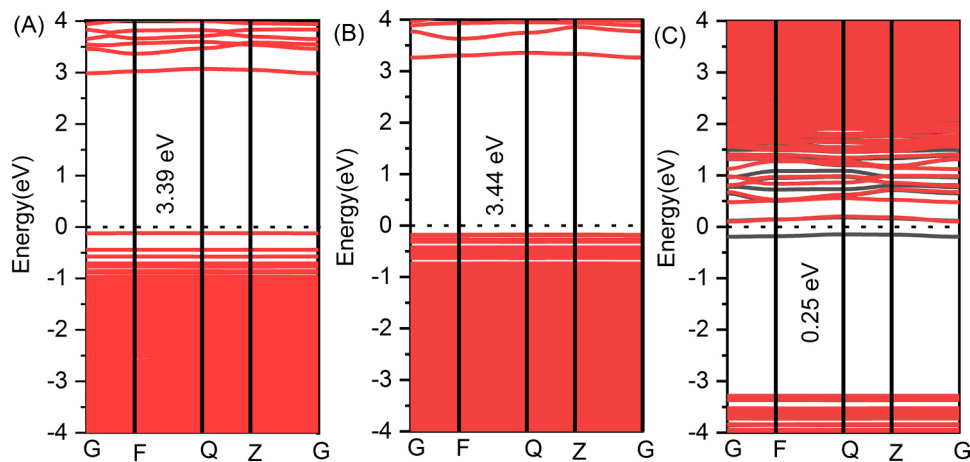


Fig. 7. Band gaps of OV-HAp with different oxygen vacancies at OV-HAp (112) crystal plane. (A) and (B) were the oxygen vacancies produced by loss an O atom in PO_4^{3-} and OH^- groups, respectively (denoted as OV-HAp-1 and OV-HAp-2). (C) Oxygen vacancies produced by the loss of the entire OH^- group in (112) plane (denoted as OV-HAp-3).

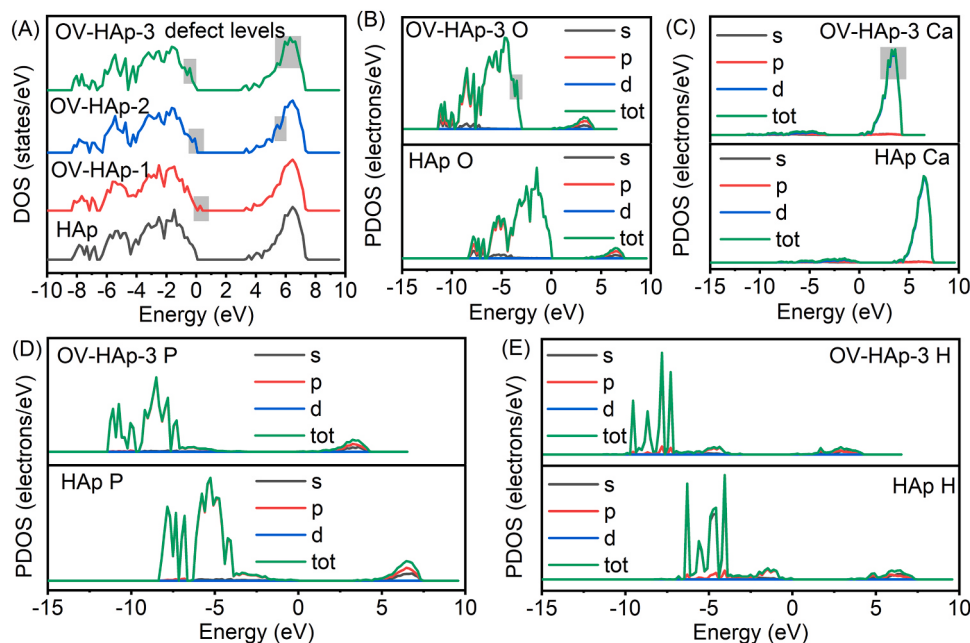


Fig. 8. Total density of states and partial density of states calculations for HAp and OV-HAp. DOS of HAp, OV-HAp-1, OV-HAp-2, and OV-HAp-3 models (A). PDOS of O, Ca, P and H atoms of HAp and OV-HAp-3 (B-E).

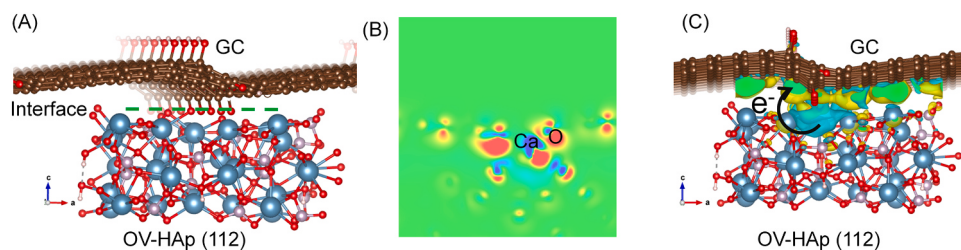


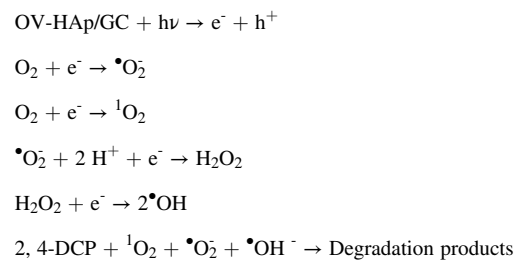
Fig. 9. Investigation of the interfacial charge transfer in OV-HAp/GC. Side view (A), electron localization function (B), and charge difference distribution (C) of the OV-HAp (112) crystal plane forming a contact interface with GC (yellow for charge accumulation and blue for charge depletion). The blue, purple, orange, red and gold spheres represented Ca, P, C, O and H atoms, accordingly.

3.5. Study of the photocatalytic degradation mechanism of 2, 4-DCP on OV-HAp/GC

The degradation mechanism of 2, 4-DCP on OV-HAp/GC catalyst was investigated through monitoring the reactive oxygen species (ROS) in the degradation process by EPR technique. No discriminable EPR signal for ROS could be observed on OV-HAp/GC catalyst under the dark environment (Fig. 10A–C). For the GC sample, there was no EPR signal under full-spectrum light irradiation for 3 min. For the OV-HAp, only the signal of DMPO- $\bullet\text{O}_2$ was observed (Fig. S21). These results demonstrated the weak ability of GC and OV-HAp for ROS generation since the photogenerated electron-hole pairs were easy to recombine. For the OV-HAp/GC, the featured triplet signal peaks of TEMP- $^1\text{O}_2$ were observed under full-spectrum light irradiation for 3 min (Fig. 10A). In addition, the quartet distinct peaks for DMPO- $\bullet\text{O}_2$ and four-line DMPO- $\bullet\text{OH}$ signal were distinctly detected after the same time irradiation (Fig. 10B–C). These results confirmed the generation of $^1\text{O}_2$, $\bullet\text{O}_2$ and $\bullet\text{OH}$ on OV-HAp/GC sample under full-spectrum light irradiation [72,73]. Moreover, the radical species trapping experiments were carried out to reveal which active species played the main role in photocatalytic degradation of 2, 4-DCP on OV-HAp/GC. Different capture agents, such as tryptophan (Trp), benzoquinone (BQ), isopropyl alcohol (IPA) and ethylenediaminetetraacetic acid disodium salt dihydrate (EDTA), were added into the OV-HAp/GC system, which were used as the quencher for $^1\text{O}_2$, $\bullet\text{O}_2$, $\bullet\text{OH}$ and h^+ , accordingly [74]. Under the full-spectrum light irradiation, as displayed in Fig. 10D, the degradation efficiency of 2, 4-DCP significantly decreased with the presence of Trp, BQ and IPA in the system, whereas it kept unchanged after EDTA addition. These indicated that $^1\text{O}_2$, $\bullet\text{O}_2$ and $\bullet\text{OH}$ determined the photocatalytic degradation of 2, 4-DCP. The similar results were founded in the OV-HAp/GC system under visible or NIR light irradiation (Fig. S22A–S22B).

Based on the above experimental results, the mechanism of ROS formation and photocatalytic degradation of 2, 4-DCP on OV-HAp/GC photocatalyst were proposed in Fig. 11. First, the CB and VB of OV-HAp under full-spectrum light irradiation generated photoelectrons and holes, respectively. The photoelectrons on the CB were rapidly

transferred to GC due to the tight interfacial connection between OV-HAp and GC. Subsequently, the photoelectrons reacted with O_2 to form $\bullet\text{O}_2$ since the E_{CB} of OV-HAp was more negative than the standard redox potential $E_0(\text{O}_2/\bullet\text{O}_2) = -0.33$ V (vs. NHE) [75]. Meanwhile, oxygen vacancies might lower the energy barrier to support the formation process of $^1\text{O}_2$, which played a non-negligible role in photocatalysis [76]. However, h^+ cannot directly oxidize OH^- or H_2O to generation $\bullet\text{OH}$ radical because the redox potential of E_{VB} was more negative than $E_0(\text{OH}^-/\bullet\text{OH}) = 1.99$ eV, $E_0(\text{H}_2\text{O}/\bullet\text{OH}) = 2.27$ eV [77]. Therefore, it speculated that the pathway of $\bullet\text{OH}$ production might be through the O_2 multiple electron reaction [78]. Finally, the degradation pathway of 2, 4-DCP on OV-HAp/GC was postulated based on the above ROS detection results and the generated intermediates during the 2, 4-DCP degradation process were detected by LC-MS (Fig. S23 and Fig. S24). The relevant reaction equations were as follows:



4. Universality research

Because of the full-spectrum response property of OV-HAp/GC prepared by the in-situ synthetic method, we applied this method to CaSiO_3 insulator modification (seen in SI 1.1–1.2, Fig. S25). The XRD, Raman and EPR results all confirmed that the obtained OV- CaSiO_3 /GC composites material had abundant oxygen vacancies (Fig. S25A–S25C). More importantly, the UV-vis DRS result showed that the OV- CaSiO_3 /GC showed the full-spectrum response (Fig. S25D), indicating the

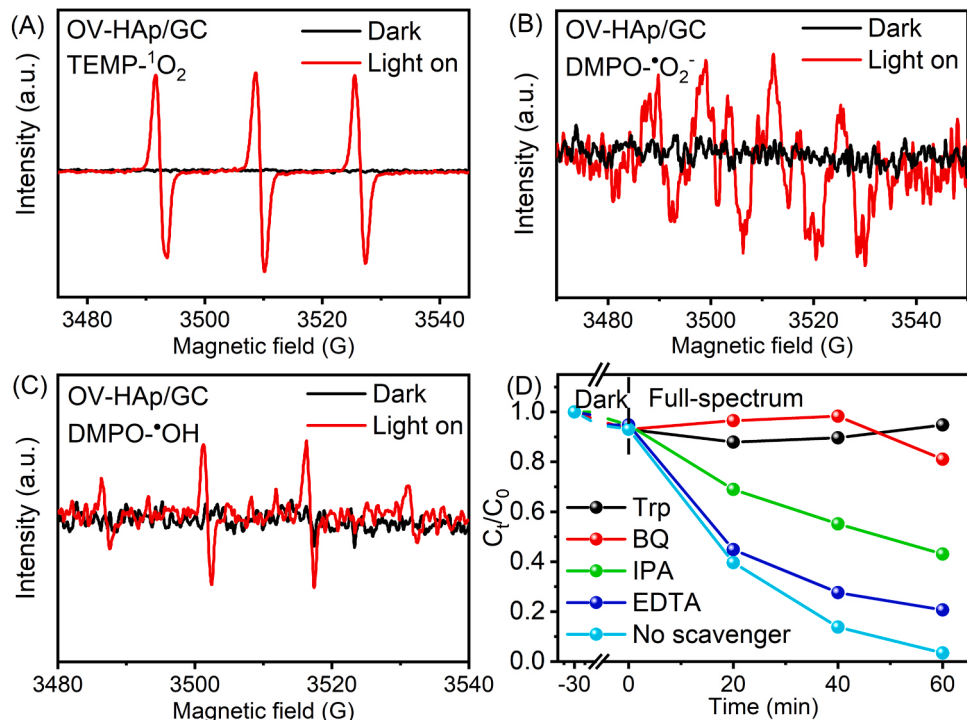


Fig. 10. Reactive oxygen species detection of the OV-HAp/GC photocatalytic system. EPR spectra of OV-HAp/GC under full-spectrum irradiation for 3 min, TEMP- $^1\text{O}_2$ (A), DMPO- $\bullet\text{O}_2$ (B) and DMPO- $\bullet\text{OH}$ (C), full-spectrum photocatalytic degradation of OV-HAp/GC with the presence of different scavenging agents (D).

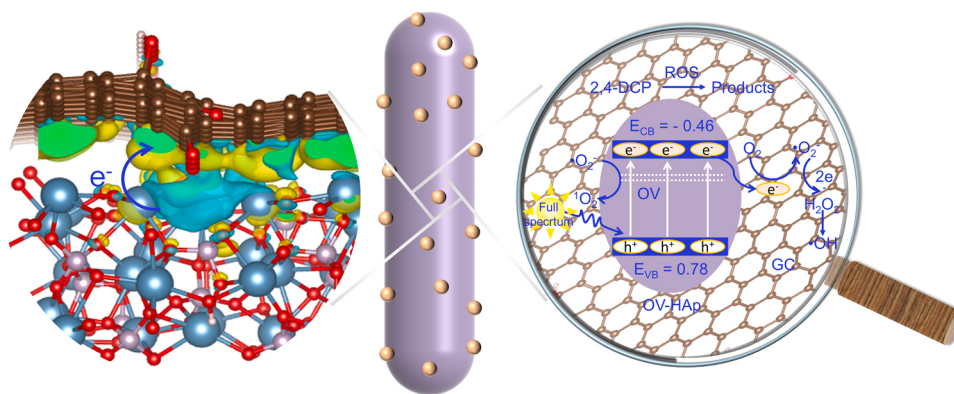


Fig. 11. Mechanism diagram of ROS formation and photocatalytic degradation of 2, 4-DCP on OV-HAp/GC.

universality of this in-situ synthetic method for improving the photocatalytic performance of the insulator materials.

5. Conclusion

In this work, the composited OV-HAp/GC photocatalyst with the full-spectrum response was constructed via coprecipitation method. The as-prepared OV-HAp/GC had abundant oxygen vacancies from loss of the OH⁻ group, which introduced a large number of defect energy levels. This resulted in the decreased band gap of OV-HAp and thus conferred it with the full-spectrum response. Besides, the interfacial interaction between OV-HAp and GC through the formation of C-O-Ca covalent bond accelerated the separation of photogenerated electron-hole pairs. These contributed to the high degradation rates for 2, 4-DCP on OV-HAp/GC under visible, NIR, and full-spectrum light, which were 1.8×10^{-3} , 9.8×10^{-4} , and 0.15 min^{-1} , accordingly. Based on these results, this material showed potential for large-scale production and practical application in future.

CRediT authorship contribution statement

Caizhi Lv: Methodology, Formal analysis, Investigation, Writing – original draft. **Pengchong Jiao:** Formal analysis, Validation. **Hui Xin:** Writing – review & editing. **Lan Wu:** Conceptualization, Writing – review & editing, Project administration, Funding acquisition. **Gangfeng Ouyang:** Writing – review & editing. **Xiandeng Hou:** Supervision.

Declaration of Competing Interest

The authors declare that they have no known competing financial interests or personal relationships that could have appeared to influence the work reported in this paper.

Data Availability

No data was used for the research described in the article.

Acknowledgements

This work was financially supported by the National Natural Science Foundation of China (No. 22276127) and the Applied Basic Research Program of Sichuan Province, China (2020YJ0246). We thank Dr. Chen Hanjiao, Dr. He Juan, Dr. Wang Shanling, Dr. Tian Yunfei and Prof. Wu Li from the Analytical & Testing Center of Sichuan University for their technical support in EPR, XRD, TEM, XPS and Raman, respectively.

Appendix A. Supporting information

Supplementary data associated with this article can be found in the

online version at [doi:10.1016/j.apcatb.2023.123248](https://doi.org/10.1016/j.apcatb.2023.123248).

References

- [1] G. Wang, B. Huang, X. Ma, Z. Wang, X. Qin, X. Zhang, Y. Dai, M.H. Whangbo, Cu₂(OH)PO₄, a near-infrared-activated photocatalyst, *Angew. Chem. Int. Ed.* 52 (2013) 4810–4813.
- [2] J. Li, X. Wu, W. Pan, G. Zhang, H. Chen, Vacancy-rich monolayer BiO_{2-x} as a highly efficient UV, visible, and near-Infrared responsive photocatalyst, *Angew. Chem. Int. Ed.* 57 (2018) 491–495.
- [3] Y. Sang, Z. Zhao, M. Zhao, P. Hao, Y. Leng, H. Liu, From UV to near-infrared, WS₂ nanosheet: a novel photocatalyst for full solar light spectrum photodegradation, *Adv. Mater.* 27 (2015) 363–369.
- [4] M.Q. Yang, L. Shen, Y. Lu, S.W. Chee, X. Lu, X. Chi, Z. Chen, Q.H. Xu, U. Mirsaidov, G.W. Ho, Disorder engineering in monolayer nanosheets enabling photothermal catalysis for full solar spectrum (250–2500 nm) harvesting, *Angew. Chem. Int. Ed.* 58 (2019) 3077–3081.
- [5] G. Li, C. Guo, M. Yan, S. Liu, Cs₂WO₃ nanorods: realization of full-spectrum-responsive photocatalytic activities from UV, visible to near-infrared region, *Appl. Catal. B Environ.* 183 (2016) 142–148.
- [6] Z. Wu, X. Yuan, H. Wang, Z. Wu, L. Jiang, H. Wang, L. Zhang, Z. Xiao, X. Chen, G. Zeng, Facile synthesis of a novel full-spectrum-responsive Co_{2.67}S₄ nanoparticles for UV-, vis- and NIR-driven photocatalysis, *Appl. Catal. B: Environ.* 202 (2017) 104–111.
- [7] X. Hu, P. Lu, M. Fu, Y. Zhang, X. Cao, J. Chen, S. Lin, J. Yao, Z. Zhang, Activating the photocatalytic activity of insulator barium silicate: a liquid-phase alkalized tetracycline photosensitizer and its self-destruction, *Chem. Eng. J.* 454 (2023) 140281–140291.
- [8] K. Li, S. Zhang, Q. Tan, X. Wu, Y. Li, Q. Li, J. Fan, K. Lv, Insulator in photocatalysis: essential roles and activation strategies, *Chem. Eng. J.* 426 (2021).
- [9] F. Dong, T. Xiong, Y. Sun, L. Lu, Y. Zhang, H. Zhang, H. Huang, Y. Zhou, Z. Wu, Exploring the photocatalysis mechanism on insulators, *Appl. Catal. B: Environ.* 219 (2017) 450–458.
- [10] M. Nishikawa, L.H. Tan, Y. Nakabayashi, T. Hasegawa, W. Shiroishi, S. Kawahara, N. Saito, A. Nosaka, Y. Nosaka, Visible light responsive vanadium-substituted hydroxyapatite photocatalysts, *J. Photochem. Photobiol. A Chem.* 311 (2015) 30–34.
- [11] V.S. Bystrov, C. Piccirillo, D.M. Tobaldi, P.M.L. Castro, J. Coutinho, S. Kopyl, R. C. Pullar, Oxygen vacancies, the optical band gap (E_g) and photocatalysis of hydroxyapatite: comparing modelling with measured data, *Appl. Catal. B: Environ.* 196 (2016) 100–107.
- [12] W.R. Leow, W.K. Ng, T. Peng, X. Liu, B. Li, W. Shi, Y. Lum, X. Wang, X. Lang, S. Li, N. Mathews, J.W. Ager, T.C. Sum, H. Hirao, X. Chen, Al₂O₃ surface complexation for photocatalytic organic transformations, *J. Am. Chem. Soc.* 139 (2017) 269–276.
- [13] Z. Liu, Z. Lu, M. Bosman, N. Li, T.J. Frankcombe, G. Jia, A. Tricoli, Y. Liu, Y. Du, Z. Yin, Photoactivity and stability co-enhancement: when localized plasmons meet oxygen vacancies in MgO, *Small* 14 (2018) 1803233–1803241.
- [14] M. Ibrahim, M. Labaki, J.M. Giraudon, J.F. Lamonier, Hydroxyapatite, a multifunctional material for air, water and soil pollution control: a review, *J. Hazard. Mater.* 383 (2020) 121139–121156.
- [15] C. Piccirillo, L.C. PM, Calcium hydroxyapatite-based photocatalysts for environment remediation: characteristics, performances and future perspectives, *J. Environ. Manag.* 193 (2017) 79–91.
- [16] N. Jiraborvornpongsa, T. Isobe, S. Matsushita, M. Oshikiri, M. Wakamura, K. Fujii, M. Yashima, A. Nakajima, Preparation and photocatalytic activity of Mo-modified Ti-doped HAp, *Appl. Catal. B: Environ.* 243 (2019) 448–454.
- [17] X. Liu, J. Ma, J. Yang, Visible-light-driven amorphous Fe(III)-substituted hydroxyapatite photocatalyst: characterization and photocatalytic activity, *Mater. Lett.* 137 (2014) 256–259.
- [18] C. Lv, H. Liang, H. Chen, L. Wu, Hydroxyapatite supported Co₃O₄ catalyst for enhanced degradation of organic contaminants in aqueous solution: synergistic

visible-light photo-catalysis and sulfate radical oxidation process, *Microchem. J.* 149 (2019) 103959–103965.

[19] C. Lv, J. Zhang, L. Wu, G. Ouyang, X. Hou, Turning hydroxyapatite from insulator to visible-light induced photocatalytic membrane through oxygen vacancy introduction and hetero-junction forming with chitosan, *Carbohyd. Polym.* 300 (2023) 120235–120244.

[20] H. Huang, D. Verhaeghe, B. Wang, B. Ghosh, H. Zhang, J. Hofkens, J.A. Steele, M.B. J. Roeffaers, Metal halide perovskite based heterojunction photocatalysts, *Angew. Chem. Int. Ed.* 61 (2022) (2022) 03261–202203273.

[21] L. Wang, B. Zhu, J. Zhang, J.B. Ghasemi, M. Mousavi, J. Yu, S-scheme heterojunction photocatalysts for CO_2 reduction, *Matter* 5 (2022) 4187–4211.

[22] X. Han, B. Lu, X. Huang, C. Liu, S. Chen, J. Chen, Z. Zeng, S. Deng, J. Wang, Novel p- and n-type S-scheme heterojunction photocatalyst for boosted CO_2 photoreduction activity, *Appl. Catal. B: Environ.* 316 (2022) 121587–121595.

[23] Y. Zhong, C. Wu, D. Chen, J. Zhang, Y. Feng, K. Xu, W. Hao, H. Ding, G. Lv, Y. Du, L. Wang, Design of lateral and vertical $\text{Bi}_4\text{O}_5\text{I}_2/\text{BiOCl}$ heterojunctions with different charge migration pathway for efficient photoredox activity, *Appl. Catal. B: Environ.* 329 (2023) 122554–122566.

[24] M. Mokhtarifar, D.T. Nguyen, M. Sakar, M. Pederferri, M. Asa, R. Kaveh, M. V. Diamanti, T.-O. Do, Mechanistic insights into photogenerated electrons store-and-discharge in hydrogenated glucose template synthesized Pt/TiO₂/WO₃ photocatalyst for the round-the-clock decomposition of methanol, *Mater. Res. Bull.* 137 (2021), 111203–111202.

[25] W. Tian, H. Zhang, X. Duan, H. Sun, M.O. Tade, H.M. Ang, S. Wang, Nitrogen- and sulfur-codoped hierarchically porous carbon for adsorptive and oxidative removal of pharmaceutical contaminants, *ACS Appl. Mater. Interfaces* 8 (2016) 7184–7193.

[26] L. Li, Y. Yan, J. Du, S. Fu, H. Liu, F. Zhao, J. Zhou, Glucose-assisted hydrothermal synthesis of plasmonic Bi deposited nested $\text{Bi}_2\text{O}_{2-x}\text{CO}_3$ photocatalysts with enhanced photocatalytic activity, *Colloid Surf. A* 583 (2019) 123946–123956.

[27] L.-W. Zhang, H.-B. Fu, Y.-F. Zhu, Efficient TiO₂ photocatalysts from surface hybridization of TiO₂ particles with graphite-like carbon, *Adv. Funct. Mater.* 18 (2008) 2180–2189.

[28] N. Jing, A.N. Zhou, Q.H. Xu, The synthesis of super-small nano hydroxyapatite and its high dsorptions to mixed heavy metallic ions, *J. Hazard. Mater.* 353 (2018) 89–98.

[29] J. Li, J. Wang, G. Zhang, Y. Li, K. Wang, Enhanced molecular oxygen activation of Ni²⁺-doped BiO₂-x nanosheets under UV, visible and near-infrared irradiation: mechanism and DFT study, *Appl. Catal. B Environ.* 234 (2018) 167–177.

[30] G. Gonzalez, C. Costa-Vera, L.J. Borrero, D. Soto, L. Lozada, J.I. Chango, J.C. Diaz, L. Lascano, Effect of carbonates on hydroxyapatite self-activated photoluminescence response, *J. Lumin.* 195 (2018) 385–395.

[31] G. Kresse, J. Furthmüller, Efficiency of ab-initio total energy calculations for metals and semiconductors using a plane-wave basis set, *Comp. Mater. Sci.* 6 (1996) 15–50.

[32] P.E. Blochl, Projector augmented-wave method, *Phys. Rev. B Condens. Matter* 50 (1994) 17953–17979.

[33] J.P. Perdew, J.A. Chevary, S.H. Vosko, K.A. Jackson, M.R. Pederson, D.J. Singh, C. Fiolhais, Atoms, molecules, solids, and surfaces: applications of the generalized gradient approximation for exchange and correlation, *Phys. Rev. B Condens. Matter* 46 (1992) 6671–6687.

[34] S. Grimme, J. Antony, S. Ehrlich, H. Krieg, A consistent and accurate ab initio parametrization of density functional dispersion correction (DFT-D) for the 94 elements H–Pu, *J. Chem. Phys.* 132 (2010) 154104–154123.

[35] C. Feng, L. Tang, Y. Deng, J. Wang, W. Tang, Y. Liu, Z. Chen, J. Yu, J. Wang, Q. Liang, Synthesis of branched $\text{WO}_3/\text{W}_{18}\text{O}_{49}$ homojunction with enhanced interfacial charge separation and full-spectrum photocatalytic performance, *Chem. Eng. J.* 389 (2020) 124474–124485.

[36] L.J. Fang, X.L. Wang, Y.H. Li, P.F. Liu, Y.L. Wang, H.D. Zeng, H.G. Yang, Nickel nanoparticles coated with graphene layers as efficient co-catalyst for photocatalytic hydrogen evolution, *Appl. Catal. B Environ.* 200 (2017) 578–584.

[37] X. Yang, X.-J. Guo, D. Zhou, J.-K. Liu, High anticorrosion properties due to electron spin polarization of hydroxyapatite with point defects, *Ind. Eng. Chem. Res.* 61 (2022) 4179–4190.

[38] Q. Chen, H. Zhou, J. Wang, J. Bi, F. Dong, Activating earth-abundant insulator BaSO₄ for visible-light induced degradation of tetracycline, *Appl. Catal. B Environ.* 307 (2022) 121182–121193.

[39] Z. Lu, J. Wang, S. Huang, Y. Hou, Y. Li, Y. Zhao, S. Mu, J. Zhang, Y. Zhao, N. B. codoped, defect-rich graphitic carbon nanocages as high performance multifunctional electrocatalysts, *Nano Energy* 42 (2017) 334–340.

[40] J. Huang, Y. Liu, Y. Liu, H. Li, Hydroxyapatite nucleated and grown on nano titania particles enhances recruitment of *Escherichia coli* for subsequent photocatalytic elimination, *Mater. Chem. Phys.* 151 (2015) 364–371.

[41] J. Li, X.-Y. Chen, R.-B. Lei, J.-F. Lai, T.-M. Ma, Y. Li, Highly thermally conductive graphene film produced using glucose under low-temperature thermal annealing, *J. Mater. Sci.* 54 (2019) 7553–7562.

[42] T.N. Jebakumar Immanuel Edison, R. Aitchudan, N. Kärthik, Y.R. Lee, Green synthesized N-doped graphitic carbon sheets coated carbon cloth as efficient metal free electrocatalyst for hydrogen evolution reaction, *Int. J. Hydron. Energy* 42 (2017) 14390–14399.

[43] T. Xu, R. Zou, X. Lei, X. Qi, Q. Wu, W. Yao, Q. Xu, New and stable g-C₃N₄/HAp composites as highly efficient photocatalysts for tetracycline fast degradation, *Appl. Catal. B Environ.* 245 (2019) 662–671.

[44] Y. Lu, J.D. Miller, Carboxyl stretching vibrations of spontaneously adsorbed and LB-transferred calcium carboxylates as determined by FTIR internal reflection spectroscopy, *J. Colloid Interface Sci.* 256 (2002) 41–52.

[45] G. Cheng, Y. Zhang, H. Yin, Y. Ruan, Y. Sun, K. Lin, Effects of strontium substitution on the structural distortion of hydroxyapatite by rietveld refinement and Raman Spectroscopy, *Ceram. Int.* 45 (2019) 11073–11078.

[46] J. Sans, M. Arnau, F. Estrany, P. Turon, C. Aleman, Regulating the superficial vacancies and OH⁻ orientations on polarized hydroxyapatite electrocatalysts, *Adv. Mater. Interfaces* 8 (2021) 2100163–2100172.

[47] Y. Xi, D. Yang, X. Qiu, H. Wang, J. Huang, Q. Li, Renewable lignin-based carbon with a remarkable electrochemical performance from potassium compound activation, *Ind. Crop. Prod.* 124 (2018) 747–754.

[48] Y.-X. An, W.-J. Qu, P.-Z. Yu, J.-G. Lü, The assembly of a composite based on nanosheet graphene oxide and montmorillonite, *Petrol. Sci.* 15 (2018) 366–374.

[49] E. Khartzadeh, S.R. Masharian, R. Yousefi, Comparison of the photocatalytic performance of S-SnSe/GO and SnSe/S-GO nanocomposites for dye photodegradation, *Mater. Res. Bull.* 135 (2021) 111127–111138.

[50] V. Nosenko, N. Strutynska, I. Vorona, I. Zatovsky, V. Dzhaban, S. Lemishko, M. Epple, O. Prymak, N. Baran, R. Ishchenko, N. Slobodyanik, Y. Pylutskyy, N. Klyui, V. Temchenko, Structure of biocompatible coatings produced from hydroxyapatite nanoparticles by detonation spraying, *Nanoscale Res. Lett.* 10 (2015) 464–470.

[51] V.J. Huerta, P. Fernández, V. Gómez, O.A. Graeve, M. Herrera, Defect-related luminescence properties of hydroxyapatite nanobelts, *Appl. Mater. Today* 21 (2020) 100822–100831.

[52] M. Adel, A. El-Maghraby, O. El-Shazly, E.-W.F. El-Wahidy, M.A.A. Mohamed, Synthesis of few-layer graphene-like nanosheets from glucose: new facile approach for graphene-like nanosheets large-scale production, *J. Mater. Res.* 31 (2016) 455–467.

[53] W. Yang, W. Yang, F. Zhang, G. Wang, G. Shao, Hierarchical interconnected expanded graphitic ribbons embedded with amorphous carbon: an advanced carbon nanostructure for superior lithium and sodium storage, *Small* 14 (2018) 1802221–1802232.

[54] S.-C. Wu, H.-C. Hsu, S.-K. Hsu, C.-P. Tseng, W.-F. Ho, Effects of calcination on synthesis of hydroxyapatite derived from oyster shell powders, *J. Aust. Ceram. Soc.* 55 (2019) 1051–1058.

[55] Q. Zhang, W. Cai, C. Zhou, R. Xu, S. Zhang, Z. Li, R. Gao, C. Fu, Electric fatigue of BCZT ceramics sintered in different atmospheres, *Appl. Phys. A Mater.* 125 (2019) 759–767.

[56] X. Hu, J. Wang, J. Wang, Y. Deng, H. Zhang, T. Xu, W. Wang, β particles induced directional inward migration of oxygen vacancies: Surface oxygen vacancies and interface oxygen vacancies synergistically activate PMS, *Appl. Catal. B Environ.* 318 (2022) 121879–121893.

[57] N. Zhang, A. Jalil, D. Wu, S. Chen, Y. Liu, C. Gao, W. Ye, Z. Qi, H. Ju, C. Wang, X. Wu, L. Song, J. Zhu, Y. Xiong, Refining defect states in $\text{W}_{18}\text{O}_{49}$ by Mo doping: a strategy for tuning N₂ activation towards solar-driven nitrogen fixation, *J. Am. Chem. Soc.* 140 (2018) 9434–9443.

[58] J. Li, C. Shu, C. Liu, X. Chen, A. Hu, J. Long, Rationalizing the effect of oxygen vacancy on oxygen electrocatalysis in Li-O₂ battery, *Small* 16 (2020) 2001812–2001823.

[59] J.J. Lovón-Quintana, J.K. Rodriguez-Guerrero, P.G. Valenca, Carbonate hydroxyapatite as a catalyst for ethanol conversion to hydrocarbon fuels, *Appl. Catal. A Gen.* 542 (2017) 136–145.

[60] Y. Luo, S. Wang, S. Guo, K. Yuan, H. Wang, M. Dong, Z. Qin, W. Fan, J. Wang, Conversion of syngas into light olefins over bifunctional ZnCe₂ZrO₄/SAPO-34 catalysts: regulation of the surface oxygen vacancy concentration and its relation to the catalytic performance, *Catal. Sci. Technol.* 11 (2021) 338–348.

[61] Q. Cao, H. Zou, D. Liu, S. Wen, X. Chen, Flotation separation of smithsonite from calcite using an amino-acid collector, *Sep. Purif. Technol.* 281 (2022) 119980–119989.

[62] C. Yang, Q. Tan, Q. Li, J. Zhou, J. Fan, B. Li, J. Sun, K. Lv, 2D/2D Ti₃C₂ MXene/g-C₃N₄ nanosheets heterojunction for high efficient CO₂ reduction photocatalyst: Dual effects of urea, *Appl. Catal. B Environ.* 268 (2020) 118738–118748.

[63] L. Wu, J. Hong, Q. Zhang, B.-Y. Chen, J. Wang, Z. Dong, Deciphering highly resistant characteristics to different pHs of oxygen vacancy-rich Fe₂Co₁-LDH/PS system for bisphenol A degradation, *Chem. Eng. J.* 385 (2020) 123620–123634.

[64] H. Li, J. Li, Z. Ai, F. Jia, L. Zhang, Oxygen vacancy-mediated photocatalysis of BiOCl: Reactivity, selectivity, and perspectives, *Angew. Chem. Int. Ed.* 57 (2018) 122–138.

[65] J. Li, Y. Li, G. Zhang, H. Huang, X. Wu, One-dimensional/two-dimensional core-shell-structured Bi₂O₃/BiO_{2-x} heterojunction for highly efficient broad spectrum light-driven photocatalysis: faster interfacial charge transfer and enhanced molecular oxygen activation mechanism, *ACS Appl. Mater. Interfaces* 11 (2019) 7112–7122.

[66] Y. Li, X. Wu, J. Li, K. Wang, G. Zhang, Z-scheme g-C₃N₄@Cs_xWO₃ heterostructure as smart window coating for UV isolating, Vis penetrating, NIR shielding and full spectrum photocatalytic decomposing VOCs, *Appl. Catal. B Environ.* 229 (2018) 218–226.

[67] Y.-Y. Yang, X.-G. Zhang, C.-G. Niu, H.-P. Feng, P.-Z. Qin, H. Guo, C. Liang, L. Zhang, H.-Y. Liu, L. Li, Dual-channel charges transfer strategy with synergistic effect of Z-scheme heterojunction and LSPR effect for enhanced quasi-full-spectrum photocatalytic bacterial inactivation: new insight into interfacial charge transfer and molecular oxygen activation, *Appl. Catal. B Environ.* 264 (2020) 118465–118479.

[68] Y. Deng, L. Tang, C. Feng, G. Zeng, Z. Chen, J. Wang, H. Feng, B. Peng, Y. Liu, Y. Zhou, Insight into the dual-channel charge-carrier transfer path for nonmetal plasmonic tungsten oxide based composites with boosted photocatalytic activity under full-spectrum light, *Appl. Catal. B Environ.* 235 (2018) 225–237.

[69] J. Xu, W. Meng, Y. Zhang, L. Li, C. Guo, Photocatalytic degradation of tetrabromobisphenol A by mesoporous BiOBr: Efficacy, products and pathway, *Appl. Catal. B Environ.* 107 (2011) 355–362.

[70] T. Saito, Y. Ishikawa, Y. Noda, T. Yokoi, Y. Oshima, A. Nakamura, K. Matsunaga, Ca-vacancy effect on the stability of substitutional divalent cations in calcium-deficient hydroxyapatite, *J. Am. Ceram. Soc.* 106 (2022) 1587–1596.

[71] V. Maurya, K.B. Joshi, Electron localization function and compton profiles of Cu₂O, *J. Phys. Chem. A* 123 (2019) 1999–2007.

[72] X. Wang, Z. Li, Y. Zhang, Q. Li, H. Du, F. Liu, X. Zhang, H. Mu, J. Duan, Enhanced photocatalytic antibacterial and degradation performance by p-n-p type CoFe₂O₄/CoFe₂S₄/MgBi₂O₆ photocatalyst under visible light irradiation, *Chem. Eng. J.* 429 (2022) 132270–132283.

[73] W. Zhao, J. Zhang, F. Zhu, F. Mu, L. Zhang, B. Dai, J. Xu, A. Zhu, C. Sun, D.Y. C. Leung, Study the photocatalytic mechanism of the novel Ag/p-Ag₂O/n-BiVO₄ plasmonic photocatalyst for the simultaneous removal of BPA and chromium(VI), *Chem. Eng. J.* 361 (2019) 1352–1362.

[74] Y. Chai, J. Ding, L. Wang, Q. Liu, J. Ren, W.-L. Dai, Enormous enhancement in photocatalytic performance of Ag₃PO₄/HAp composite: a Z-scheme mechanism insight, *Appl. Catal. B Environ.* 179 (2015) 29–36.

[75] O. Sacco, V. Vaiano, W. Navarra, C. Daniel, S. Pragliola, V. Venditto, Catalytic system based on recyclable Fe₀ and ZnS semiconductor for UV-promoted degradation of chlorinated organic compounds, *Sep. Purif. Technol.* 270 (2021) 118830–118840.

[76] H. Zhao, X. Liu, Y. Dong, Y. Xia, H. Wang, A special synthesis of BiOCl photocatalyst for efficient pollutants removal: new insight into the band structure regulation and molecular oxygen activation, *Appl. Catal. B Environ.* 256 (2019) 117872–117880.

[77] M.S. Hosseini, A. Abbasi, M. Masteri-Farahani, Improving the photocatalytic activity of NH₂-UiO-66 by facile modification with Fe(acac)₃ complex for photocatalytic water remediation under visible light illumination, *J. Hazard. Mater.* 425 (2022) 127975–127990.

[78] Y. Nosaka, A. Nosaka, Understanding hydroxyl radical (•OH) generation processes in photocatalysis, *ACS Energy Lett.* 1 (2016) 356–359.